sciendo
Austrian Journal of Earth Sciences | Vienna | 2025 | Volume 118 | 189–203 | DOI: 10.17738/ajes.2025.0011

Seismic velocity structure and seismotectonics of the southern Vienna Basin (Austria) with a large-N nodal deployment

Clement Esteve[1*], Jeremy M. Gosselin[2], Yang Lu[3], Götz Bokelmann[1] and Gregor Götzl[4]

1) Department of Meteorology and Geophysics, University of Vienna, Vienna, 1090, Austria
2) Natural Resources Canada, Geological Survey of Canada - Pacific, Sidney, V8L 4B2, Canada
3) Department of Geosciences and Geography, University of Helsinki, Helsinki, 00560, Finland
4) EVN Wärme GmbH, Maria Enzersdorf, 2344, Austria
*) Corresponding author: clement.esteve@univie.ac.at

Keywords: Seismic tomography, machine learning, sedimentary basin, detection

Abstract

In spring 2024, we deployed a large seismic nodal array across the southern Vienna Basin, Austria. Using a machine-learning approach, we constructed a seismic catalog for the 60-day deployment period and reliably identified 100 events. We applied a local earthquake tomography inversion procedure to relocate the detected events and derive three-dimensional P- and S-wave velocity models and V_P/V_S estimates. The results reveal a low-velocity anomaly with high V_P/V_S estimates, corresponding to the Neogene basin structure. In contrast, high-velocity anomalies with low V_P/V_S estimates highlight nappe systems associated with the Alpine Orogen. Most of the relocated seismicity during the deployment is linked to the April 14th, 2024, M ~ 3 earthquake. The mechanism for this event, along with its aftershock distribution, suggest that the rupture occurred on a normal splay fault of the Vienna Basin Transfer Fault System, situated near its intersection with the basal detachment at depth. As this area is highlighted for its geothermal resource potential, a comprehensive understanding of geological structures and potential hazards is essential for responsible resource development.

1. Introduction

The Vienna Basin lies at the junction of the Eastern Alps, the Pannonian Basin, and the western Carpathians (Fig. 1a). It is a geologically complex region shaped by ongoing tectonic activity. The regional seismic activity is moderate, with instrumentally recorded earthquakes reaching a maximum magnitude of approximately 5. The Vienna Basin Transfer Fault System (VBTFS) is a 380-km long left-lateral strike-slip fault system, which is thought to be rooted on the basal detachment of the Alpine-Carpathian orogenic wedge at depths of 8 to 12 km (Hinsch et al., 2005). The VBTFS generates earthquakes exceeding magnitude 4 (Hinsch and Decker, 2011). A notable example is the magnitude 5 Ebreichsdorf event in 1938. Seismicity is well-observed in the southern Vienna Basin, but is almost absent in the central and northern Vienna Basin (Hinsch and Decker, 2011). In addition to instrumentally recorded events, historical (e.g., Gutdeutsch et al., 1987), and paleoseismological investigations (Hintersberger et al., 2010) suggest that the region has experienced even stronger earthquakes in the past, albeit less frequently.

Understanding the subsurface structure of the Vienna Basin, along with potential sources of significant earthquakes, is of particular importance. The Vienna Basin is identified as a key target for deep geothermal resources in Austria, with several projects at various stages of development (Sachsenhofer et al., 2025). In particular, geothermal exploration in the southern Vienna Basin is still in exploratory stages. For these projects, understanding the seismotectonics of the area is crucial for accurately assessing seismic hazards before proceeding with further planning and development.

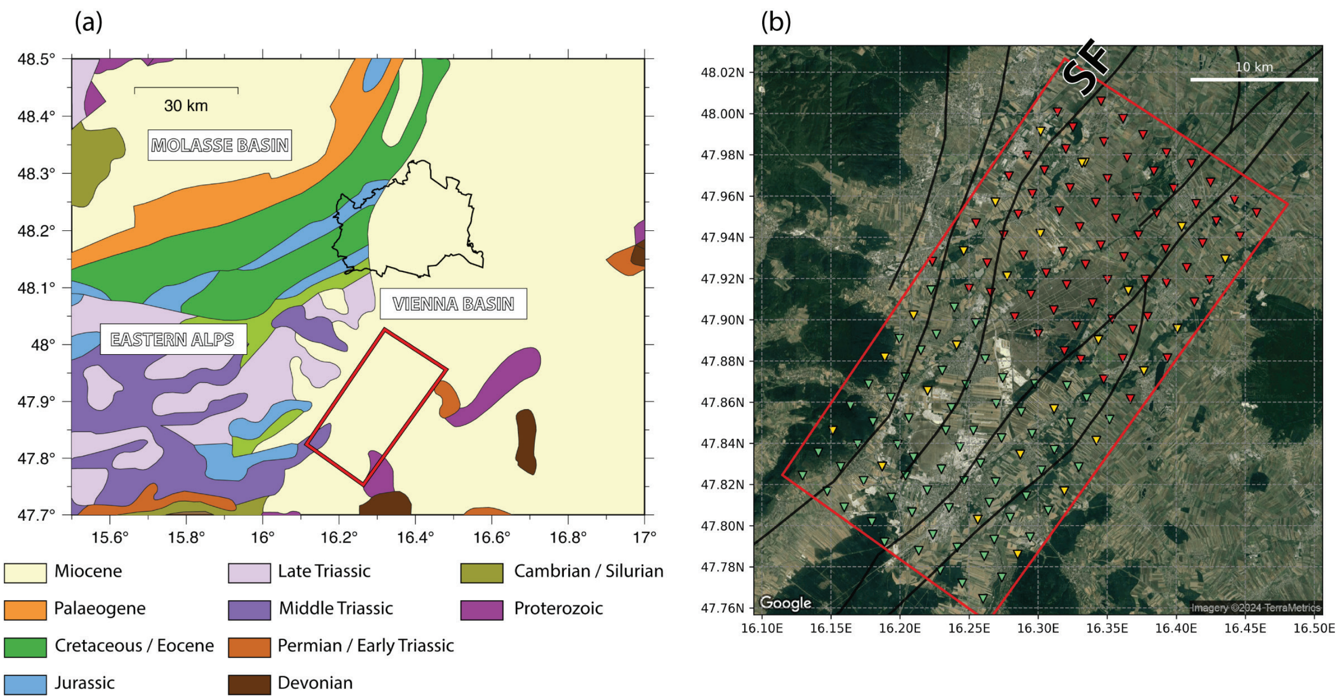

Figure 1: (a) Surface geology of eastern Austria extracted from the International Geological Map of Europe (IGME5000; Aschk, 2005). **(b)** Satellite image of the southern Vienna Basin. The red box shows the extent of the study area. Inverted green and red triangles show the first and second phase of the seismic survey, respectively. Inverted yellow triangles represent seismic nodal sensors common to the two phases of the seismic survey. Black solid lines show mapped tectonic faults in the area. Abbreviations: SF = Sollenau Fault.

Recent studies have demonstrated that large-N, short-duration, seismic nodal arrays can detect a significantly higher number of small seismic events compared to what are listed in national earthquake catalogs, which rely on regional networks (e.g., Catchings et al., 2020; Shearer et al., 2024). Seismic phase arrival times can then be determined from these small events and used in a local earthquake tomography inversion procedure (e.g., Dunham and Kiser, 2020) to improve our understanding of the local seismic velocity structure and local deformation in a given region.

In this study, we deployed a large seismic nodal array across the southern Vienna Basin, and constructed a seismic catalog using a machine-learning (ML) algorithm. We then picked the seismic phase arrival times associated to the detected events and employed a local earthquake tomography inversion procedure for determining the seismic velocity structure of the area and refine the earthquake hypocentral locations. Finally, we interpret our results in the context of the active seismotectonics of the southern Vienna Basin, highlighting how the observed active fault geometries and deformation patterns relate to the deeper structure. Our findings provide new insights into the basin's seismogenic behavior and have direct implications for seismic hazard assessment and geothermal resource development in the region. More broadly, our study demonstrates how dense nodal arrays and advanced processing techniques can illuminate the detailed structure and activity of fault systems in complex tectonic settings, providing a framework for similar investigations in other intraplate basins worldwide.

2. Data and Method

2.1. Data

We deployed 181 seismic nodal sensors in two asynchronous phases across the southern Vienna Basin (Fig. 1b). In the first phase, 90 sensors were installed in the southern half of the study area, recording seismic data between March 18th to April 24th, 2024. The second phase involved the deployment of 91 sensors to the northern half of the study area, recording seismic data from May 6th to June 19th, 2024. Out of a total of 181 deployed seismic nodal sensors, 4 failed to record. Except for the failed nodal sensors, all sensors recorded continuously for more than 30 days. All seismic nodal instruments are *Fairfield Nodal Zland* three-component (north, east, and vertical) nodes with a 5-Hz corner frequency.

To build the seismic catalog, we employed SeisBench, a user-friendly interface that applies several standard seismological machine-learning (ML) algorithms (Woollam et al., 2022). Prior to processing the continuous waveform data, we apply detrending, demeaning and downsampling of the data to 25 Hz. SeisBench scans through hourly seismic segments. Here, we used EQTransformer (Mousavi et al., 2020) to generate ~ 40,000 preliminary detections. Figure 2 shows an example of a 300-second vertical component seismogram for station 101 (see Fig. 3 for location) starting at 3:10:00 PM on April 14th, 2024, alongside the predictions of P- and S-wave arrival times by PhaseNet (Zhu and Beroza, 2019) and EQTransformer. Note that event detections are performed by EQTransfomer.

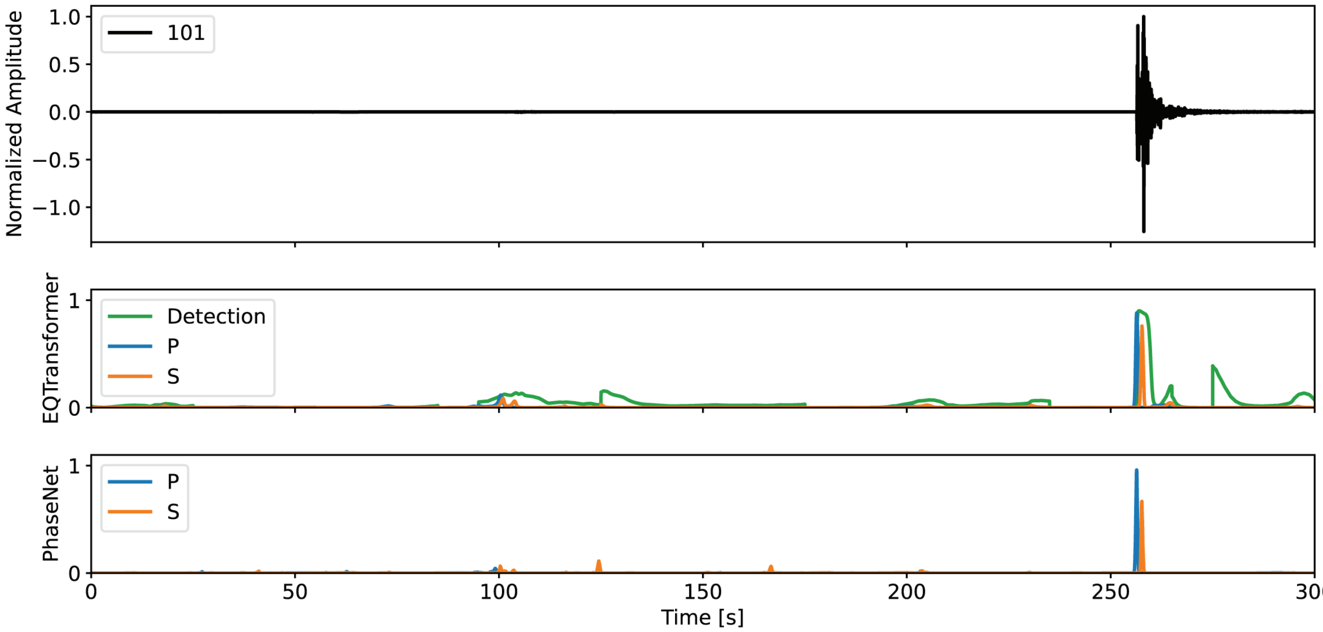

Figure 2: The top panel shows a 300-second vertical-component seismogram of the seismic node 101 (see Fig. 3). The bottom two panels show the characteristic curves (i.e., probability of a seismic phase pick at a given time) for the two models EQTransformer (Mousavi et al., 2020) and PhaseNet (Zhu and Beroza, 2019). Note that only EQTransformer detects events.

To associate the event detection to the corresponding phase arrival times, we used an earthquake phase association algorithm, GaMMA (Zhu et al., 2022). This requires an initial P- and S-wave velocity models. Here, we used an average 1-D shear-wave velocity model from Esteve et al. (2025). We then converted the S-wave velocity model to a P-wave velocity model assuming a constant V_P/V_S ratio of 1.75 (Tab. T1 in the supplementary material). Because of the large number of recording seismic sensors, we only kept events with at least 10 associated P- and S-wave phase arrivals associated to this particular event. After this quality control process, we were left with 100 reliable events to use in subsequent analysis (Fig. 3).

Due to the limited number of detected events, we decided to manually re-pick the P- and S-wave arrival times in order to ensure accurate identification of phase onsets. To improve the clarity of seismic phase arrivals, we applied a Butterworth band-pass filter with a 1–12 Hz frequency band to correctly determine P and S phases for each seismogram. In total, we measured 2298 and 2234 P- and S-wave arrival times, respectively. This arrival time data set, along with the event hypocentral locations, is the input to the tomographic inversion procedure (Fig. S1).

Lastly, for comprehensive analysis of our constructed catalog, we determine local earthquake magnitudes (M_L) for each event using a local magnitude scale defined for central Europe (Chovanová and Kristek, 2018), where is described as:

$$M_L = \log A + 1.05 * \log(\Delta_{ij}) + 0.00236 * \Delta_{ij} - 2.02$$

Here, A is the maximum amplitude in nanometers, Δ_{ij} is the epicentral distance in kilometers. We note that local magnitude (M_L) estimates derived from the 5 Hz short-period sensors deployed in our nodal array are likely subject to systematic underestimation. The original M_L scale was calibrated using Wood-Anderson seismographs, which have a flat response in the 1–10 Hz band and greater sensitivity to the longer-period energy radiated by larger or more distant earthquakes. In contrast, 5 Hz sensors attenuate much of the low-frequency signal, effectively acting as a high-pass filter. In this study, M_L values are therefore reported as indicative lower bounds.

2.2. Inversion procedure

We use the Local Tomography Software (LOTOS) to estimate the three-dimensional isotropic seismic velocity structure (Koulakov, 2009). LOTOS has been successfully applied to a wide range of settings (e.g., Schmid et al., 2017; Estève et al., 2022; Koulakov et al., 2023; Jiwawi-Brown et al., 2024). Starting with a 1–D (i.e., layered) velocity model, the software calculates the travel times based on a reference table of initial event locations, and uses a grid search method to relocate all events (Koulakov and Sobolev, 2006). We use the term “relocation” to distinguish between the ML locations and our final locations. Ray paths are updated using a three-dimensional bending ray tracing method (Um and Thurber, 1987), with the velocity model and event hypocenters updated at each iteration. The same 1-D reference velocity model used for the earthquake phase association is used as the initial model in the LOTOS inversion.

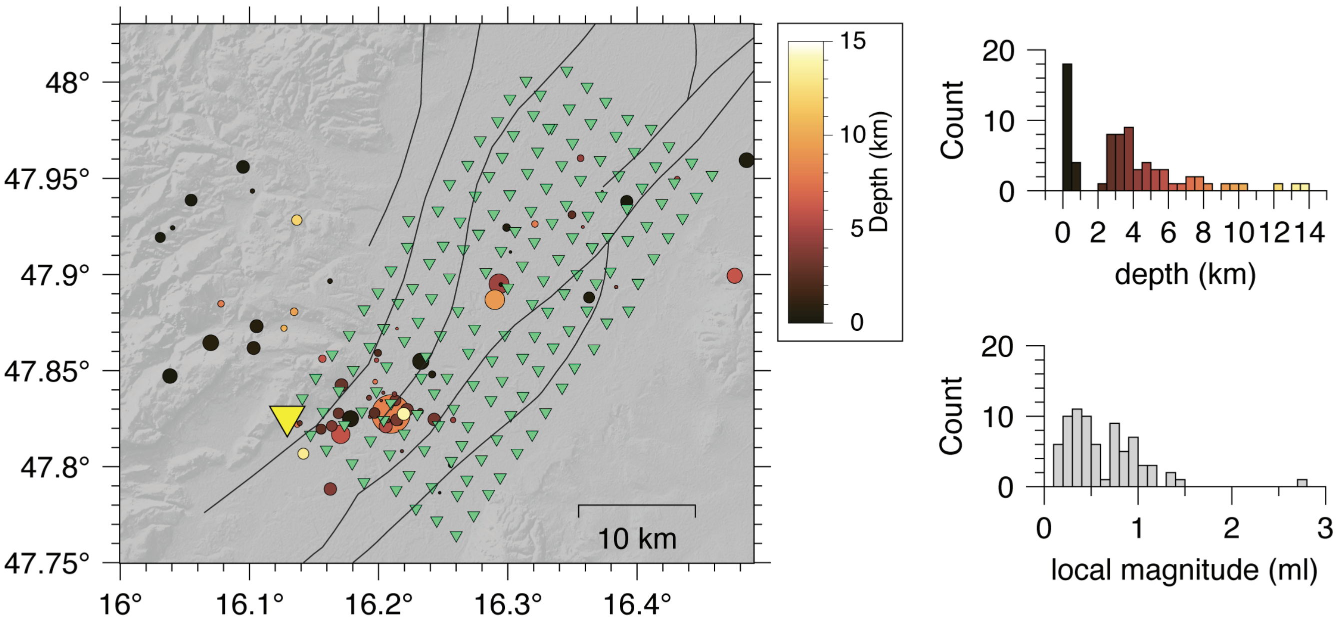

Figure 3: Map showing all events detected and located by the ML algorithm. Yellow inverted triangle shows the location of the seismic node 101. Each event is color-coded by depth and the circle size correspond to the magnitude. Two histograms show the distribution of preliminary hypocentres determined by the ML algorithm and the range of local magnitude.

P-wave and S-wave arrival times are simultaneously inverted for P and S-wave velocity anomalies using an iterative LSQR algorithm (Paige and Saunders, 1982). Earthquake hypocenters are refined for each model iteration. Many tomographic studies use trade-off curves (L-curves) to find the best regularization parameters. However, the study of Koulakov (2009) has shown that the damping value computed in this way may not be appropriate. First, the L-curve is often computed for the first iteration of the inversion procedure. At the same time, the main results of these studies are obtained after performing several iterations. The damping parameters obtained as corner points of the L-curve do not necessarily coincide in the first and final iterations. It would be more reasonable to use the value that corresponds to the L-curve in the final iteration, but in this case, the problem becomes too time-consuming. Second, even if we use a damping value corresponding to the L-curve in the final iteration, it is not clear that this value is really optimal. Koulakov, (2009) has tested this question with several synthetic models, and he has observed that damping estimated in this way is too strong. Therefore, the performance of synthetic modelling gives the best chance to estimate the free parameters. Successively, the parameters can be adjusted in order to improve the quality of the synthetic anomalies. The values of the parameters are refined by performing successive tests. We use smoothing and damping parameters of 0.3 and 1.0, respectively, for both the P- and S-wave velocity models. These optimal values were selected by evaluating synthetic tests and RMS time residuals.

We used 5 iterations to derive the final velocity models, as RMS time residuals no longer significantly decrease for subsequent iterations (Tab. T2 in the supplementary material). The mean deviations of the residuals were reduced from 0.1226 to 0.0624 s (49 %) for the P-wave data set and from 0.2371 to 0.0983 s (58.5 %) for the S-wave data set. In the following sections, we only show the southern part of the study area, as the northern part is poorly sampled (Fig. S2).

Both the P- and S-wave velocity models are parameterized using a set of nodes, which depend on the ray path density (Fig. S2). The spacing between nodes is 0.8 km and 0.5 km in the horizontal and vertical directions, respectively, in areas with sufficient ray path density. Between the nodes, velocity anomalies (from the reference model) are linearly interpolated. To minimize artifacts related to the geometric distribution of nodes and ray geometry, we perform the LOTOS inversion using four grid with different azimuths (0°, 22°, 45° and 67°; Fig S3). Each grid orientation is constructed during the first iteration and remains unchanged throughout subsequent iterations. This approach resulted in four comparable three-dimensional velocity models, increasing our confidence that grid orientation did not introduce significant artifacts. The final velocity model is obtained by averaging the four three-dimensional velocity models generated from these different grid orientations.

2.3. Focal mechanism calculation

Earthquake source characteristics provide valuable constraints on fault geometry and processes, and represent an important contribution to understanding earthquake hazards. We investigate the source characteristics

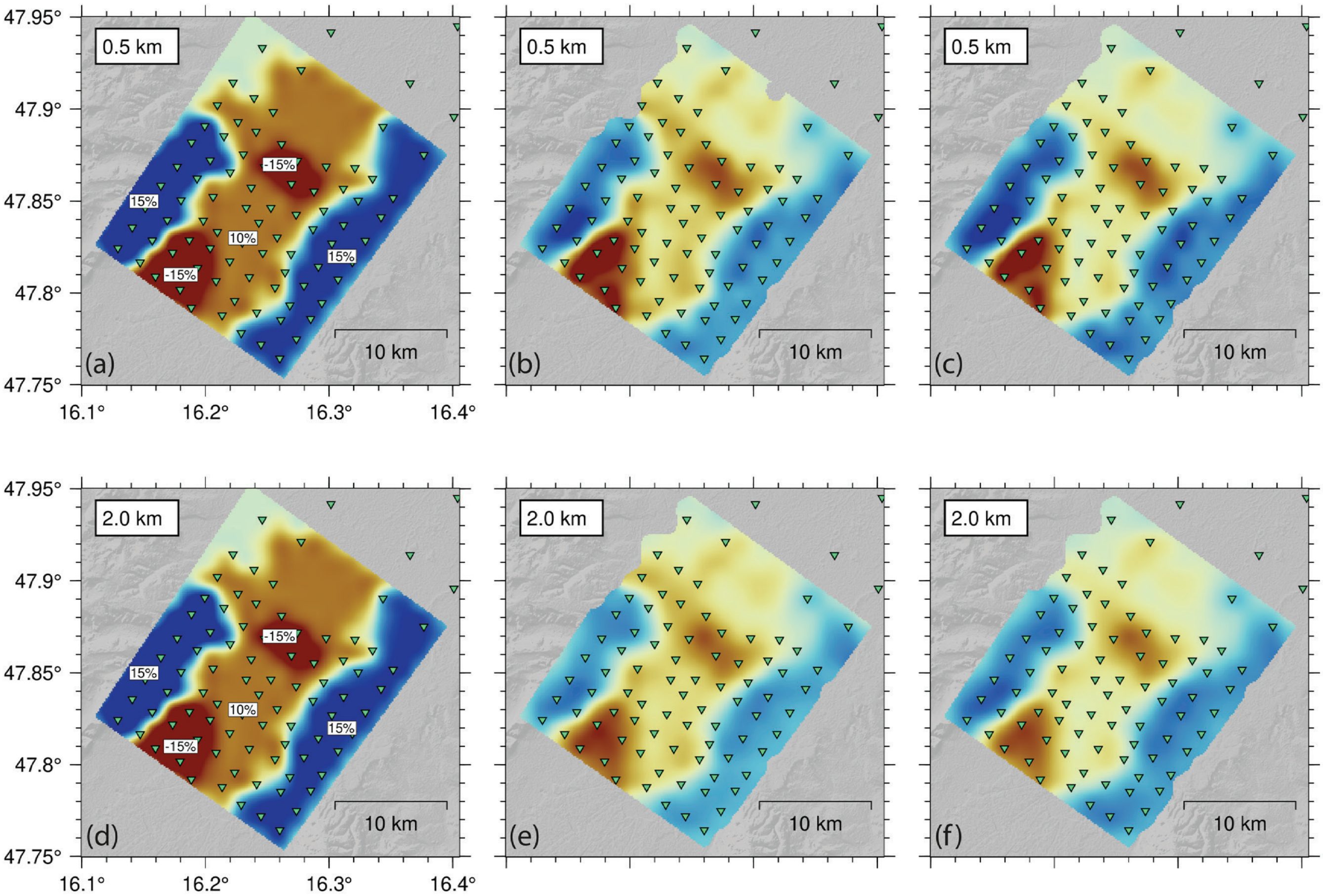

Figure 4: Synthetic tests with realistic anomalies in map view at depths of 0.5 and 2 km for both P- and S-wave models. The original synthetic model with the P- and S-wave velocity anomalies are presented **(a, d)**, and the recovered structure through the P- **(b, e)** and S-wave velocity model **(c, f)** for the same parameters are shown. The values of the P- and S-wave velocity anomalies in percent in the synthetic model are indicated inside each pattern.

of the largest event identified from our detection analysis: a $M_L \sim 3$ event that occurred on April 14th, 2024. Specifically, we manually pick the P-wave first-motion polarities (i.e., dilational or compressional) recorded on our nearly 90 nodal instruments, and invert these to determine a probabilistic focal mechanism solution. The nodal planes from this solution are then interpreted within the context of previously mapped regional faults, as well as our tomographic model of seismic velocity structure of the southern Vienna Basin. Unfortunately, we are not able to analyze the remaining (much smaller) event due to low signal-to-noise ratio and our inability to manually pick a sufficient number of clear first-motion polarities.

Using the hypocentral location from our iterative tomography and earthquake relocation process, we calculate azimuths and takeoff angles based on the average 1-D velocity model from Esteve et al. (2025). With this information (polarities, takeoff angles, and azimuths) we apply the Bayesian Earthquake Analysis Tool (BEAT) software (Vasyura-Bathke et al., 2020; Gosselin et al., 2023) to estimate the probability distributions of the focal mechanism parameters. The BEAT subpackage used for focal mechanism inversion does not yet support take-off angle calculations with a 3D velocity model. We consider event location uncertainties to be the dominant source of error in take-off and azimuth angles. BEAT allows for rigorous quantification of the uncertainties in the estimated focal mechanism allowing for more reliable interpretation within the context of faults and earthquake hazards. Within the inversion, the data and focal mechanism model parameters are both treated as random variables. The model parameters are constrained by the data as well as prior information. However, in this work, we employ uninformative priors to allow the solution to be constrained by data information content. We define the prior as bounded uniform distributions over the range of physically possible angles of strike (0–360 degrees), dip (0–90 degrees), and rake (–180–180 degrees). This allows the solution to be defined by the polarity data. It is challenging to determine an analytical solution for the probability distribution of the focal mechanism parameters. Instead, BEAT relies on numerical methods to draw samples from the posterior distribution. The ensemble of samples can then be used as an approximation of the posterior distribution, as well as to estimate its properties.

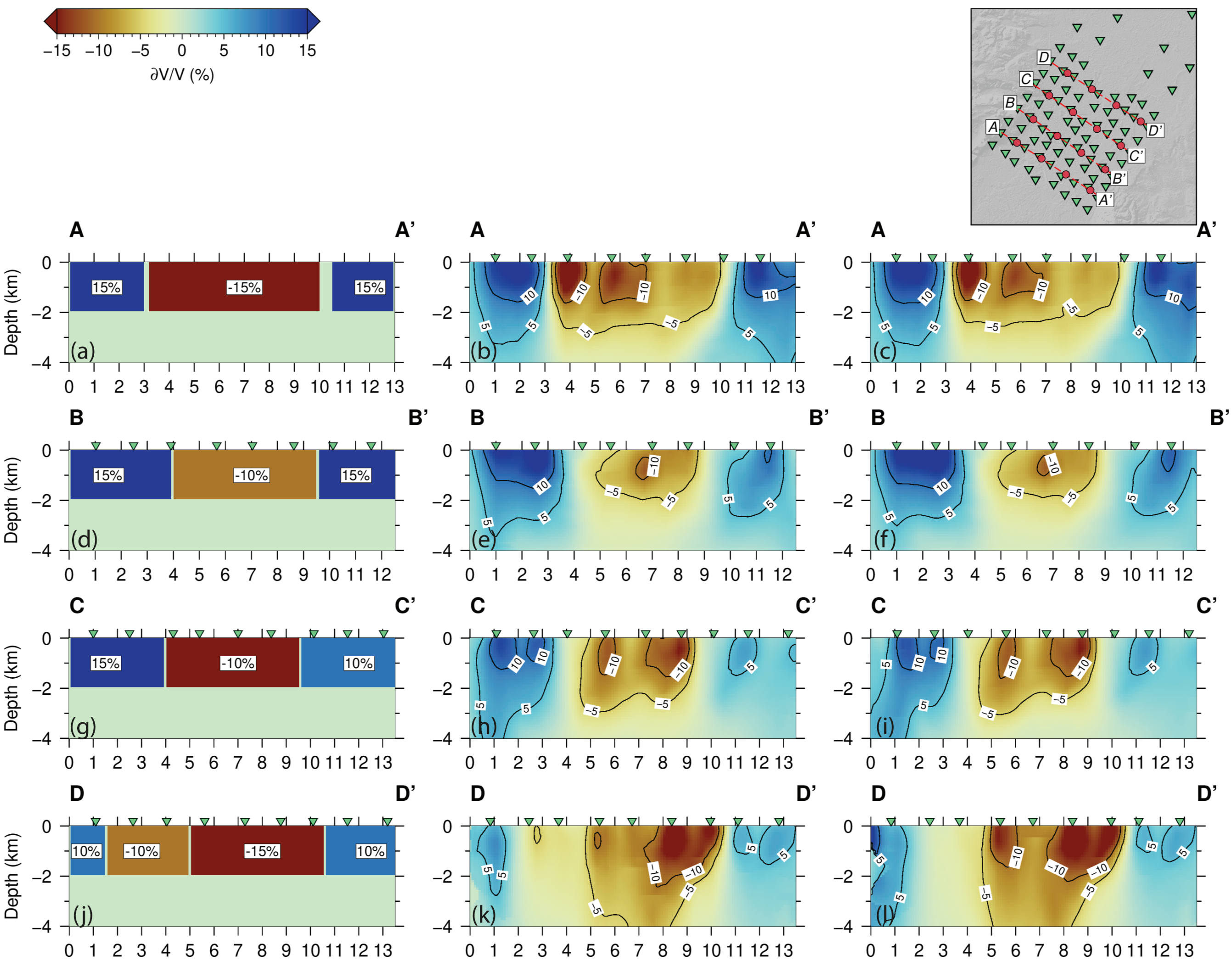

Figure 5: Synthetic tests with realistic anomalies defined along vertical profiles. Input synthetic anomalies along the vertical profiles **(a, d, g, j)**. Recovered P- **(b, e, h, k)** and S-wave velocity models **(c, f, i, l)** along the same profile. For profile locations, refer to inset map.

3. Model resolution

We conduct synthetic checkerboard and structural tests to evaluate the resolution of our tomography models. The test models feature an alternating pattern of fast and slow velocity anomalies, with amplitudes set at ±10% of the background velocity. These tests were designed for two configurations, where each anomaly measures either 5 x 5 x 5 km (Figs. S4–S6) or 2 x 2 x 2 km (Figs. S7–S9). Synthetic travel times are calculated using 3D ray tracing, and noise levels are defined as 5% and 10% of the real remnant residual values to simulate travel-time errors in the initial P- and S-wave datasets, respectively. Following the computation of synthetic data, we apply the full inversion procedure, including earthquake relocations, to determine which parts of the model are best resolved. This synthetic inversion effectively replicates real data processing (Koulakov, 2009). After the final iteration, the average source relocation error is 0.95 km (Fig. S10), while event relocation errors for events located beyond the extent of the nodal array are larger due to the limited azimuthal range in station coverage for these events (Fig. S10).

Figure S4 to S9 present the results of the checkerboard tests for 2-km and 5-km anomalies, respectively. The recovered models reveal a clear variation in resolution with increasing depth. In the top 2 km, the synthetic anomalies are well retrieved in both tests, with preserved amplitudes and shapes. However, at depths beyond 2 km, the 2-km anomalies are poorly resolved due to insufficient crossing rays in our dataset. In contrast, the 5-km anomalies remain detectable, although their amplitude recovery is less accurate. The checkerboard resolution tests suggest that the seismic velocity models can resolve 5-km lateral anomalies beneath the nodal array to a depth of 4 km, while 2-km lateral anomalies can be resolved to depths of 2–2.5 km.

In addition to the checkerboard test, we evaluate the resolution of longer-wavelength features and the impact of limited resolution in our real model by conducting synthetic structural tests with realistic anomalies (Figs.

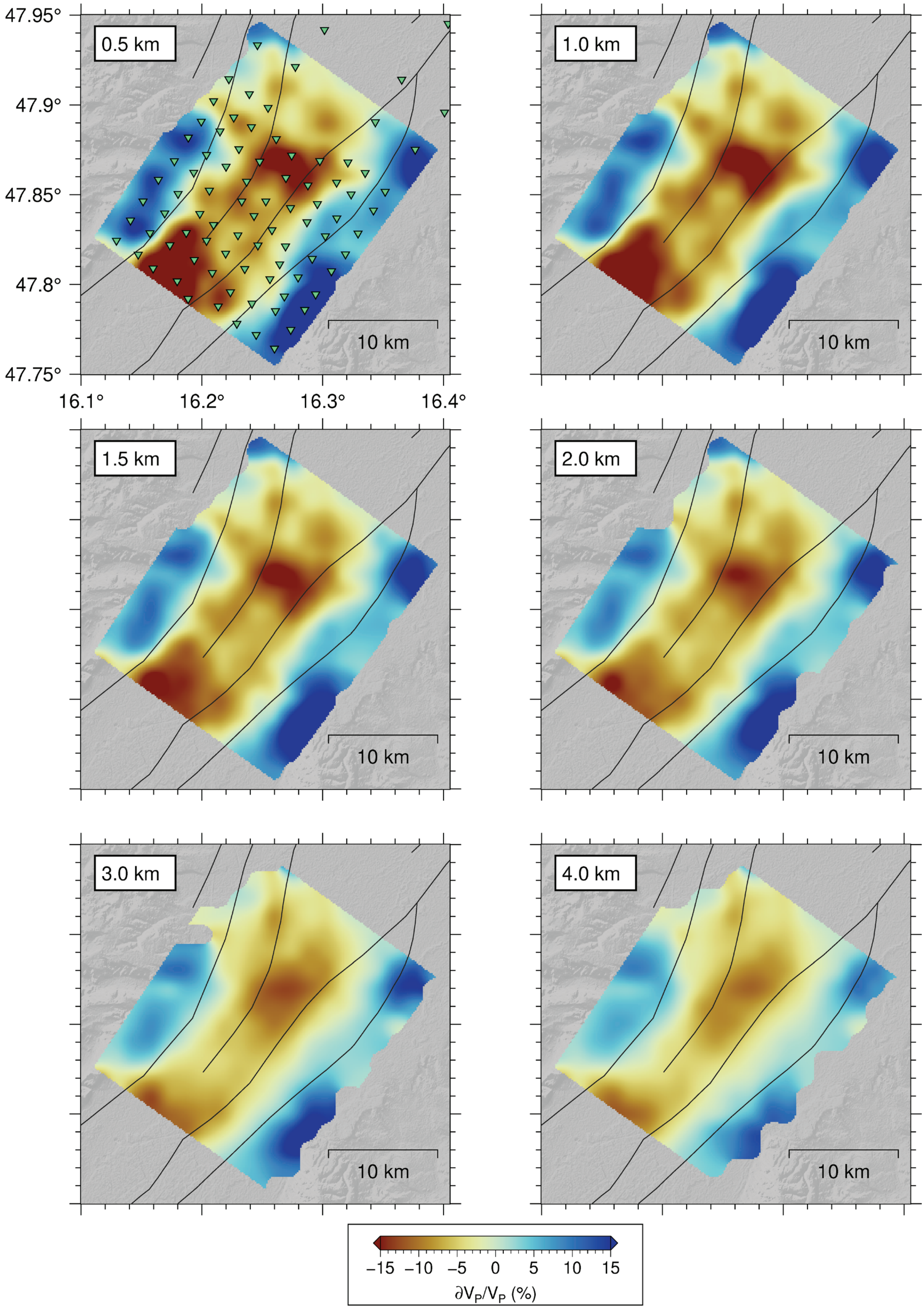

Figure 6: Map views of the P-wave model at depths of 0.5, 1, 1.5, 2, 3 and 4 km. Inverted green triangles show the seismic nodal instrument locations. Black lines show the mapped faults in the area.

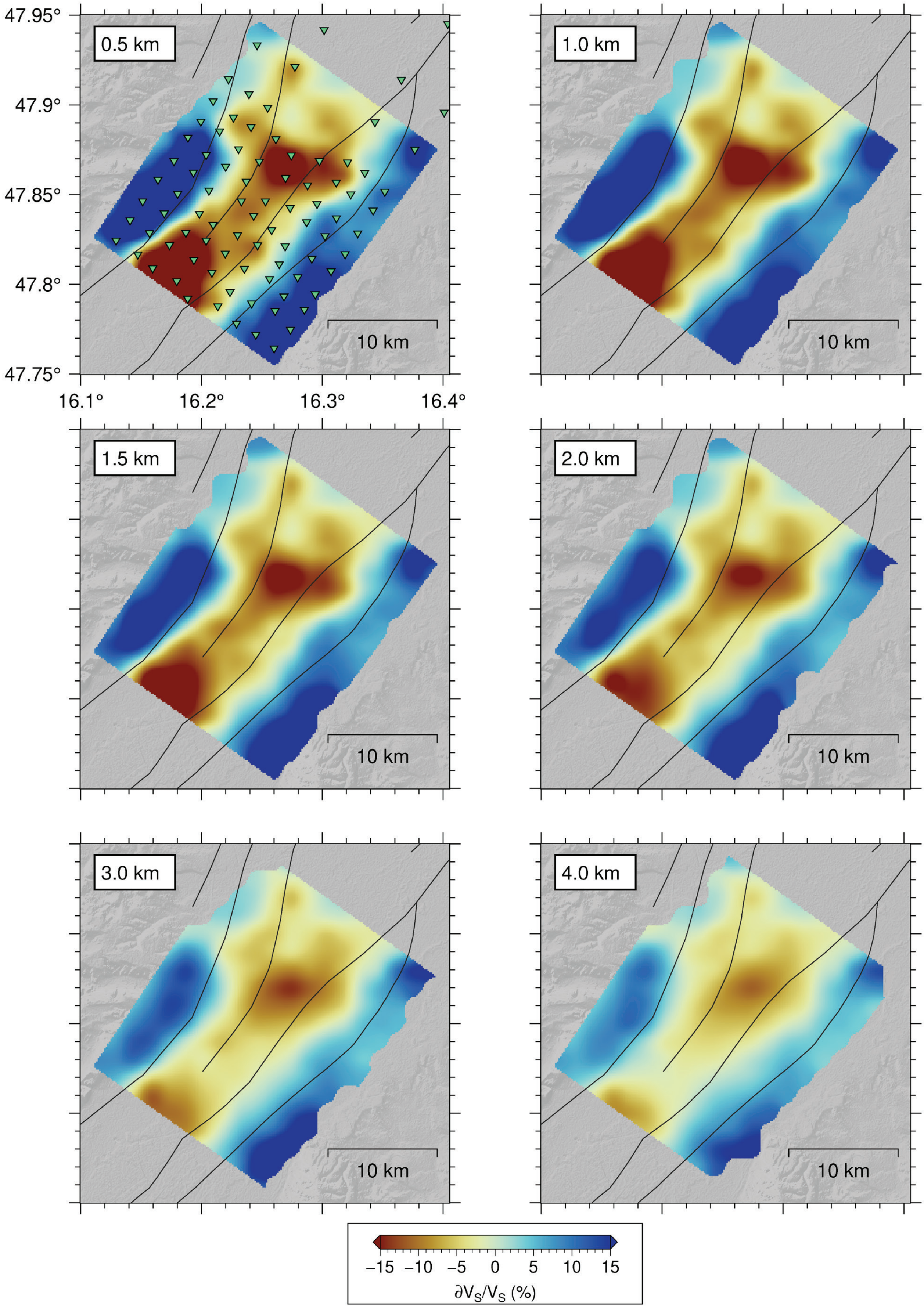

Figure 7: Map views of the S-wave model at depths of 0.5, 1, 1.5, 2, 3 and 4 km. Inverted green triangles show the seismic nodal instrument locations. Black lines show the mapped faults in the area.

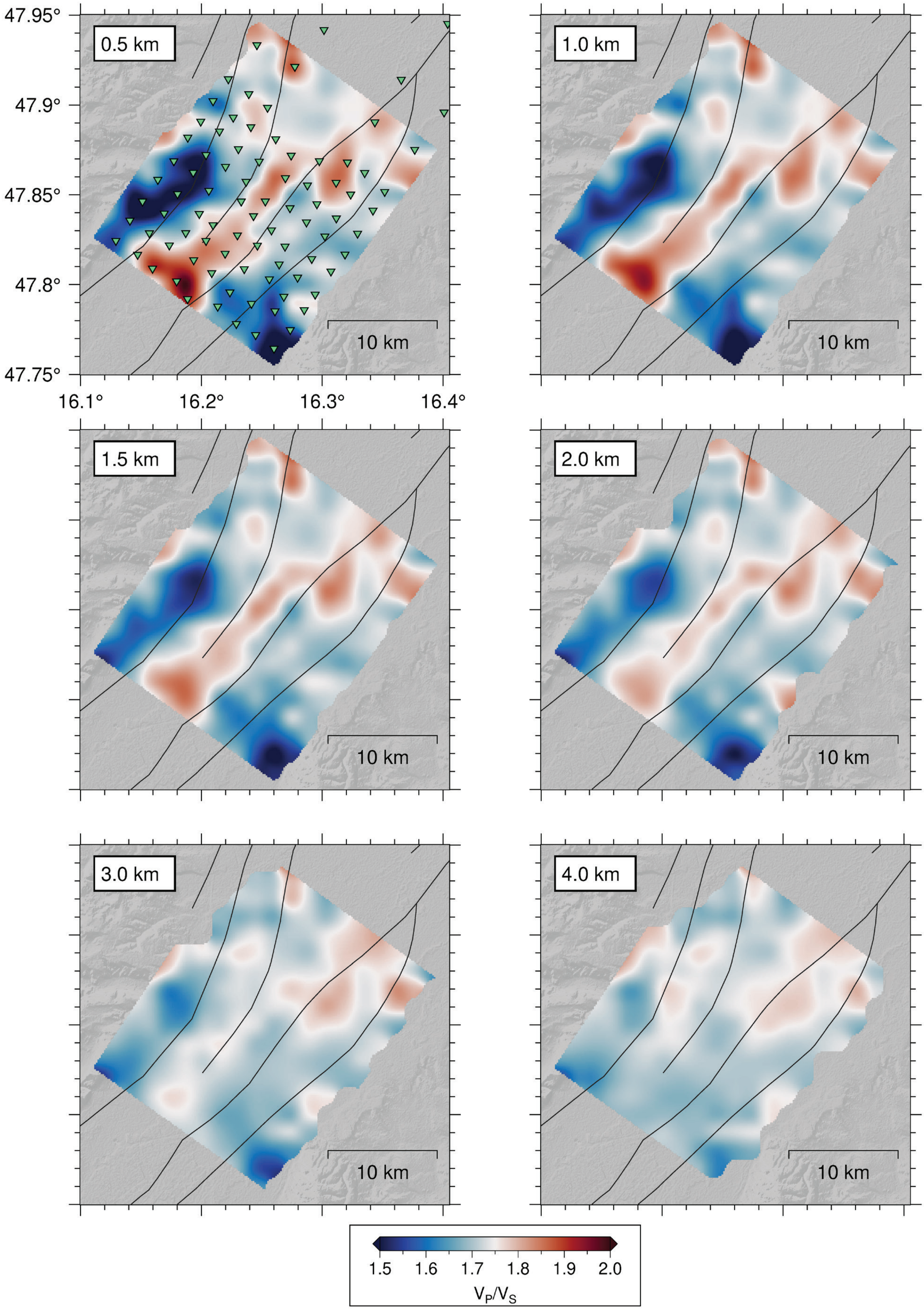

Figure 8: Map views of the V_P/V_S model at depths of 0.5, 1, 1.5, 2, 3 and 4 km. Inverted green triangles show the seismic nodal instrument locations. Black lines show the mapped faults in the area.

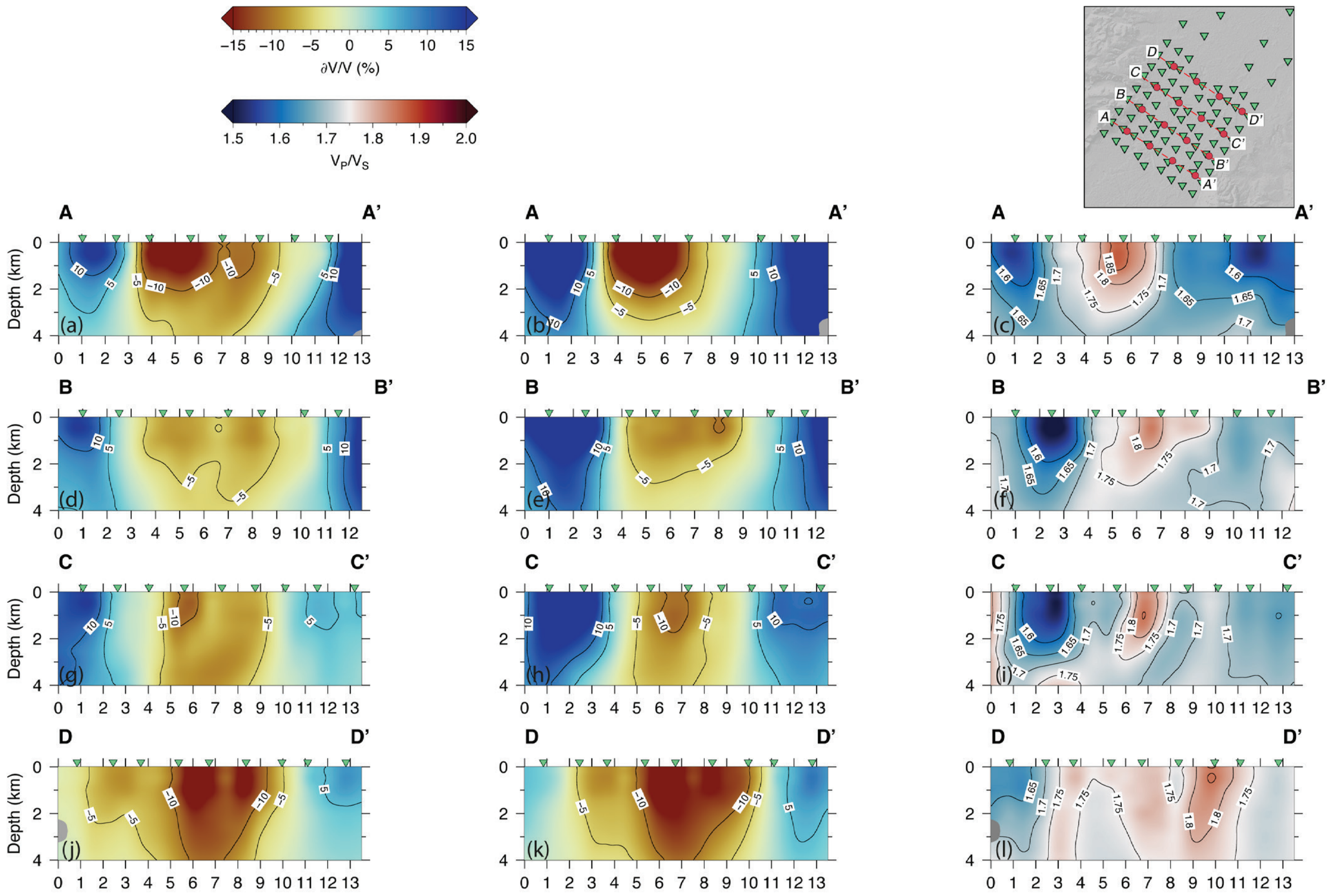

Figure 9: Vertical profiles through the P-wave **(a, d, g, j)**, S-wave **(b, e, h, k)** and V_P/V_S models **(c, f, i, l)**.

4, 5). This test incorporates structures that replicate key features observed in the recovered model (see following section) and follows the same procedure used in the checkerboard resolution tests. In map view, the anomalies are well recovered in the top 2 km. However, the amplitude recovery for both P- and S-wave models is approximately 50–60%, which is typical for regularized (specifically, damped) tomographic models. In vertical view, the lateral extent of the synthetic anomalies is accurately retrieved, though vertical smearing effects are evident in both P- and S-wave models.

4. Results

4.1. P- and S-wave velocity anomalies and V_P/V_S estimates of the southern Vienna Basin

We present depth slices and vertical profiles through the P-wave, S-wave and V_P/V_S models of the southern Vienna Basin (Figs. 6–8). We show other vertical profiles in the supplementary information (Figs. S11–S14). The P- and S-wave velocity depth slices and vertical profiles are plotted as perturbations relative to the reference 1-D velocity model ($\delta V/V$). For both P- and S-wave velocity models, we see that the central region is characterized by a low-velocity anomaly. Notably, two sub-regions are characterized by slower velocities ($\delta V/V$ <10 %). The western and eastern edges of both models are characterized by high-velocity anomalies.

V_P/V_S estimates range between 1.5 and 2.0 and the distribution appears to correlate spatially with the velocity anomalies (Figs. 8, 9). In the top 2 km beneath the surface, we identify a northwest-southeast belt within the central part of the study area with V_P/V_S >1.8 corresponding to the low-velocity P- and S-wave anomalies. The western and eastern edges are characterized by V_P/V_S <1.7 and correspond to high-velocity P- and S-wave anomalies.

4.2. Relocated seismicity and source characteristics

Figure 10 shows the relocated seismicity within the study area during the deployment period (March 21st to June 19th, 2024). After relocations, we see that most of the earthquakes occur at depths ranging between 7 and 11 km (Fig. 10a). We also note that 16 events occurred at depths shallower than 1 km and mainly occur in the eastern Alps in two small clusters. These two locations correspond to quarries. Consequently, we interpret these events to be associated with industrial activity. We also show the distribution of events over the period of

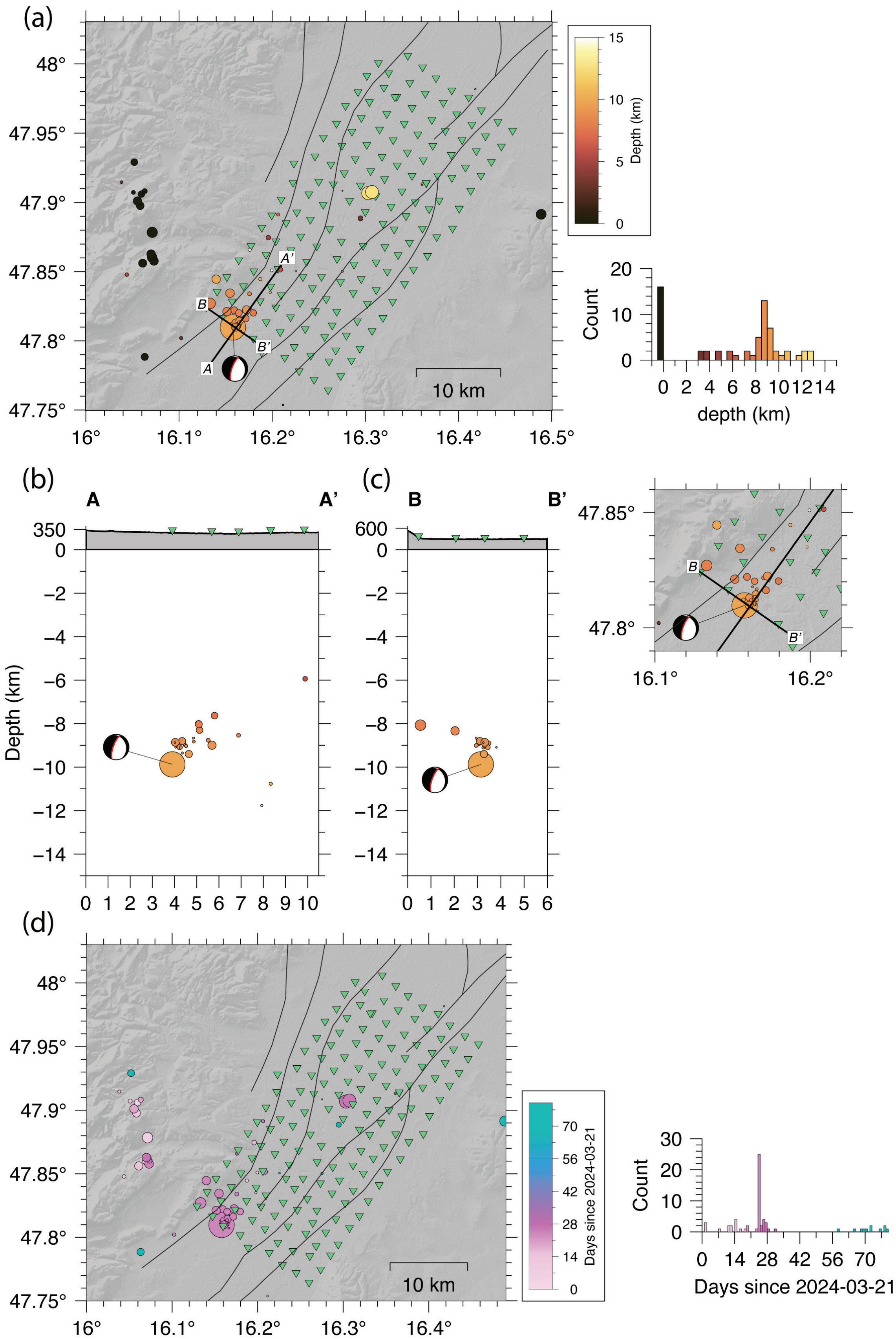

Figure 10: (a) Relocated events in the final three-dimensional models. Each event is color-coded by depth. Focal mechanism solution for the April 14th, 2024, $M_L \sim 3$ earthquake. The fault plane is highlighted in red. Histogram shows the depth distribution of those relocated events. **(b-c)** Vertical profiles AA′ and BB′ centred on the relocated $M_L \sim 3$ earthquake cluster with the focal mechanism solution. **(d)** Relocated events color-coded by occurrence since the beginning of the seismic survey (March 21st, 2024) in map view and histogram.

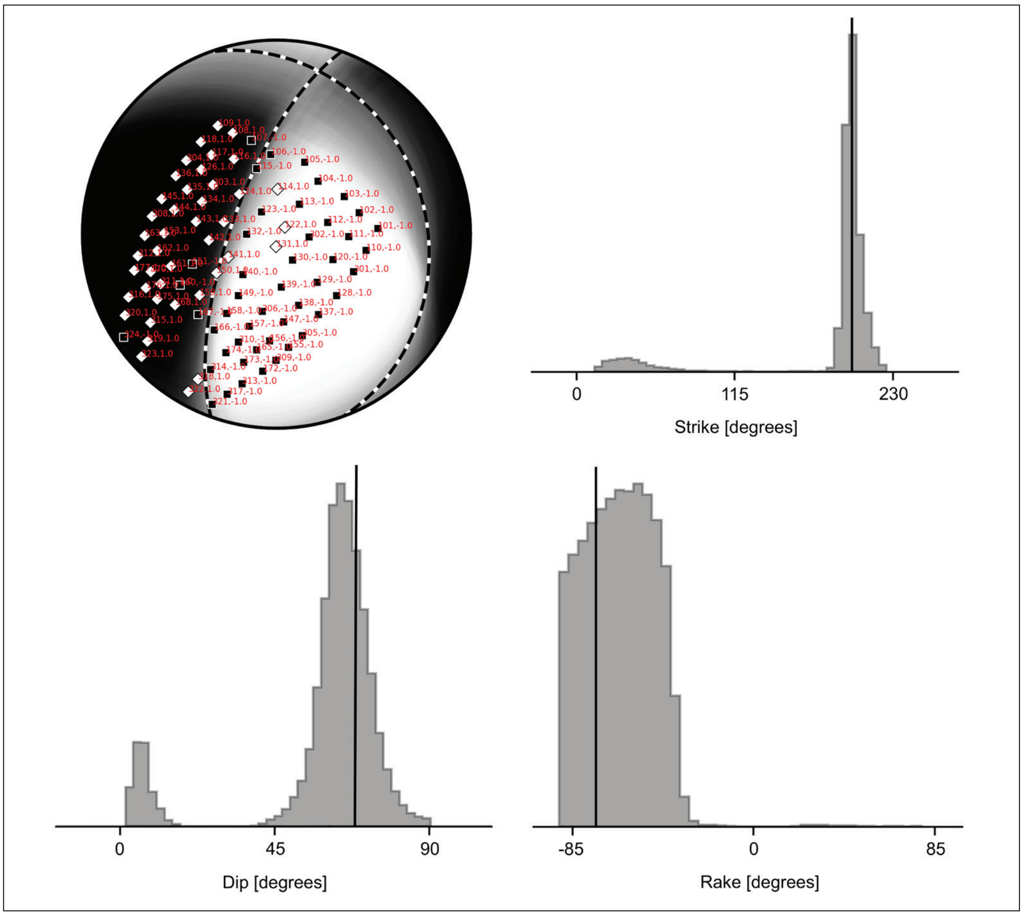

Figure 11: Bayesian focal mechanism inversion from polarity data. Inversion results are shown for the April 14th, 2024, $M_L \sim 3$ earthquake. The 'fuzzy beachball' is shown for an ensemble of 200 focal mechanisms drawn from the posterior probability density (top left). White diamonds and black squares represent positive and negative polarity data, respectively, located at the modelled azimuth and take-off angles. The marginal posterior distributions are also shown for the strike, dip and rake of one of the mechanism planes. Vertical lines in the marginal distribution plots identify the location of the maximum probability model.

our experiment (Fig. 10d), and highlight that most of the detected seismicity occurred between April 10th to 20th (20–30 days into the experiment), likely associated with the largest event in our catalog: the $M_L \sim 3$ earthquake on April 14th. We show vertical profiles centered on the $M_L \sim 3$ earthquake sequence (Fig. 10b-c), and note that our relocated seismicity defines a cluster between 8 and 10 km depth.

Figure 11 shows the results of our probabilistic focal mechanism inversion for the April 14th $M_L \sim 3$ event. A focal mechanism solution is typically represented by a beachball diagram representing the stereonet projection of the lower half of the focal sphere. An advantage of the approach adopted in our work is rigorous uncertainty quantification, which we illustrate visually by a fuzzy beachball diagram. This represents an ensemble of 200 focal mechanism samples drawn from the posterior probability distribution. The sharpness (and fuzziness) of the image provides qualitative assessment of uncertainty. We also show the marginal probability distributions for strike, dip, and rake of this event, which represent the highest probability focal mechanism solution and uncertainties. Lastly, we show the manually selected polarity data on our focal mechanism solution, which clearly delineate one of the mechanism nodal planes with only a few erroneous polarity picks.

5. Discussion

5.1. The southern Vienna Basin seismic velocity structure and its surroundings

We identify a low P- and S-wave velocity anomaly and high V_P/V_S estimates (Figs. 6–9) extending from the surface to a depth of 3–4 km. This anomaly forms a northeast-southwest-oriented, belt-like structure. Synthetic tests with realistic anomalies indicate that vertical smearing affects the features observed in our models, preventing us from precisely determining the base of this anomaly (Figs. 4, 5). Nonetheless, we observe a strong correlation between the lateral extent of the Neogene basin and the low-velocity anomaly. Additionally, P- and S-wave velocities corresponding to this low-velocity anomaly range between 2.2–3.6 km/s and 1.0–2.0 km/s,

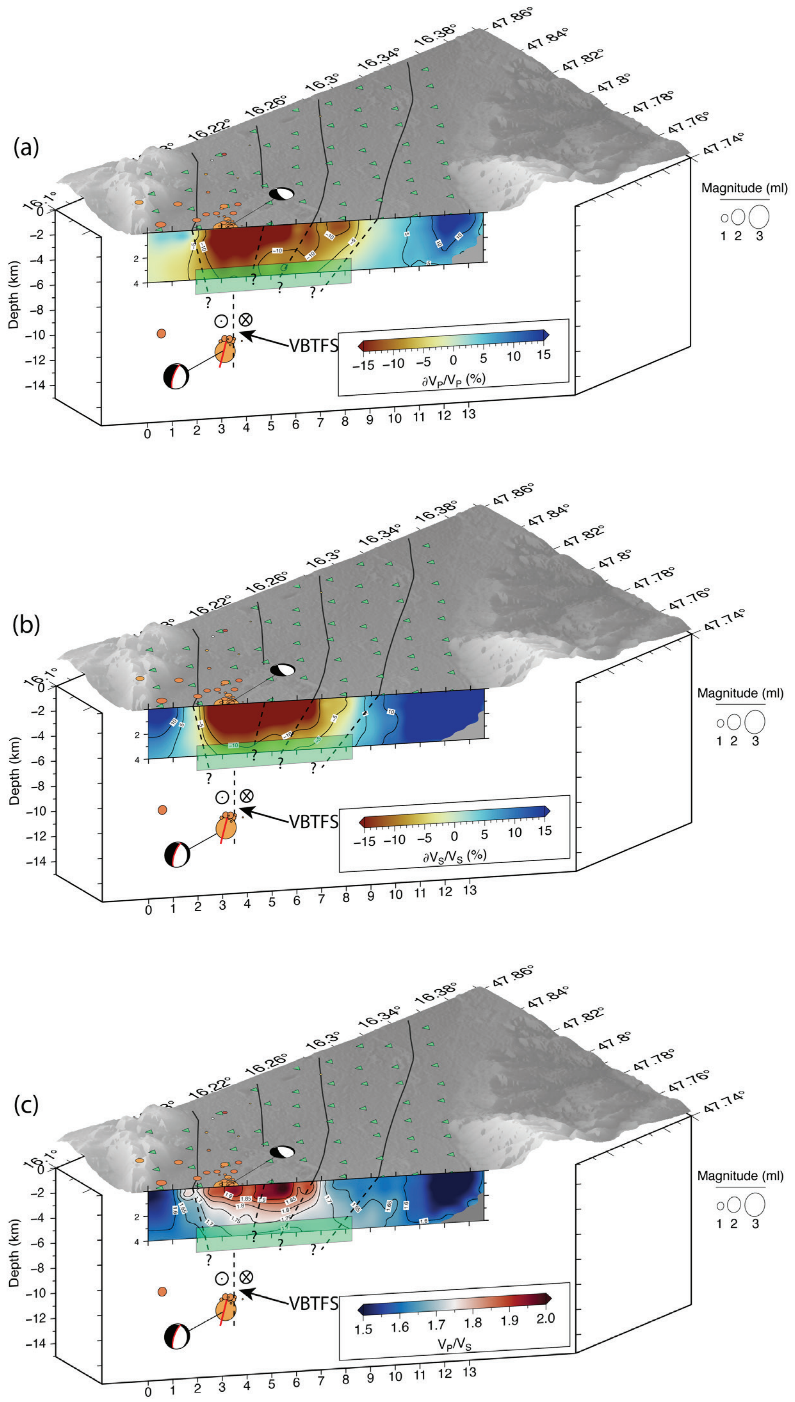

Figure 12: Conceptual view of the V_P **(a)**, V_S **(b)**, V_P/V_S **(c)** models and relationship with seismicity in the southern Vienna Basin. The Neogene basin is highlighted by the slow seismic velocities and high V_P/V_S estimates, while the Alpine nappe systems is characterized by fast seismic velocities and low V_P/V_S estimates. The cluster of seismicity occurred beneath the flower structure of the VBTFS (green rectangle, Decker et al. 2005) and the April 14th, 2024, M_L ~ 3 earthquake is likely associated with a west-northwest-dipping normal splay fault of the VBTFS.

respectively (Figs. S15–S16). These P- and S-wave velocities correspond to sandstone, shale, limestone (Schön, 2015). Furthermore, the low-velocity feature identified in our local earthquake tomography aligns well with findings from a recent ambient-noise tomography of the southern Vienna Basin (Esteve et al., 2025). Based on this agreement, we interpret the low-velocity anomaly as representing the extent of the Neogene basin.

The western and eastern edges of the study area exhibit high P- and S-wave velocity anomalies, corresponding to low V_P/V_S estimates (Figs. 6–9). In the west, the local geology is associated with the Alpine Orogen, specifically the Tirolic-Noric nappe system, which comprises limestones, dolomites, and sandstones (Froitzheim et al., 2008). To the east, the lithologies are also linked to the Alpine Orogen but belong to the Semmering-Wechsel nappe system, consisting of marble, quartzite, dolomite, and meta-conglomerate (Froitzheim et al., 2008). P- and S-wave velocities corresponding to these high-velocity anomalies range between 3–5.2 km/s and 1.8–3.0 km/s, respectively (Figs. S15–S16). These seismic velocities correspond to limestone, sandstone, quartzite, schist, gneiss (Schön, 2015). Therefore, we interpret the high P- and S-wave velocities as the seismic signature of the lithologies associated to the local Alpine nappe systems.

5.2. The April 14th, 2024, $M_L \sim 3$ earthquake in the southern Vienna Basin

After relocations, we see that the seismicity associated with the April 14th, 2024, $M_L \sim 3$ earthquake defines a cluster (Fig. 10). Hypocentral depths of these events range between 8 and 10 km, which is in good agreement with earthquake studies in eastern Austria (Apoloner et al., 2014; Hausmann et al., 2010; Lenhardt et al., 2007). Apoloner et al. (2014) relocated a 2013 earthquake sequence that occurred in the southern Vienna Basin. They obtained an average hypocentral depth of 9 km and interpreted these hypocenters to be located beneath the base of the flower structure associated to the VBTFS. The obtained focal mechanism solution for the April 14th, 2024, $M_L \sim 3$ earthquake indicates a steep (~70°) fault plane with normal faulting, which can be related to the VBTFS or one of the associated splay faults. Furthermore, the distribution of hypocenters coincides with the junction between the VBTFS and the basal detachment (Decker et al., 2005; Hinsch et al., 2004). Both the strike and steep dip from the focal mechanism solution align well with the surface expressions of tectonic structures within the area and with focal mechanism solutions determined from regional seismic networks (as summarized in Levi et al., 2024). Based on these observations, we suggest that the April 14th, 2024, $M_L \sim 3$ earthquake is likely associated with a west-northwest-dipping normal splay fault of the VBTFS, situated near its intersection with the basal detachment. The observation of this moderate normal-faulting event suggests that some structures within, or associated with, the VBTFS occupy locally favorable stress regimes for fault-hosted geothermal resources. Additional observations, including focal mechanism estimates, could help refine crustal stress in the area. The occurrence of this moderate event near the resource target reinforces the need for additional study on seismic hazards prior to future development.

6. Conclusion

We successfully deployed a large seismic nodal array across the southern Vienna Basin in spring 2024. Using a machine-learning algorithm, we constructed a seismic catalog for the deployment period. Preliminary locations show that most of the detected seismicity occurred beneath the array at depths ranging from the surface to 15 km, with preliminary local magnitude estimates ranging from 0.1 to 3. We then manually picked the seismic phase arrival times for these events and applied local earthquake tomography for determining the seismic velocity structure of the area and refine the event locations. Figure 12 shows a conceptual model of the obtained seismic velocity models (V_P, V_S and V_P/V_S) and relationship with seismicity and tectonic structures in the southern Vienna Basin. The resulting seismic velocity models highlight the structure of the Neogene basin, and the nappe systems associated with the Alpine Orogen. Most of the relocated epicenters are clustered beneath the southwestern end of the array at depths of 8 to 10 km. We extend our analysis by inverting P-wave first-motion polarity data to infer the focal mechanism of the largest event in this cluster, which reveals that the rupture occurred on a steeply dipping normal fault. We suggest that this cluster of seismicity occurred beneath the flower structure of the VBTFS and that the April 14th, 2024, $M_L \sim 3$ earthquake is likely associated with a west-northwest-dipping normal splay fault of the VBTFS, situated near its intersection with the basal detachment. Our observations of active motion on these structures have implications for the regional tectonics, seismic hazards, and resource development in the area. Continued dense monitoring and integrated geological–geophysical studies will be essential to fully resolve the activity and potential of other fault segments in this complex tectonic setting.

Acknowledgements

We thank Stefan Weiginger, Florian Bleibinhaus, as well as Bastian Joachim-Mrosko and Kurt Stüwe for their comments and suggestions, which improved the quality of the manuscript. We gratefully acknowledge funding from *EVN Wärme GmbH*. The authors wish to thank Daniel Schützenhofer, Yongki Aiman, Jonas Mohideen and Tobias Jirec in assisting all aspects of the field experiment. The authors also thank the villages, towns, and landowners for permitting the deployment of several seismic nodes. We thank Ivan Koulakov for providing the tomography software and guidance. We acknowledge Kurt Decker for insightful conversations on the tectonics of the Vienna Basin. Figures were created using *Generic Mapping Tools* (Wessel et al., 2013).

References

Apoloner M-T., Bokelmann G., Bianchi I., Brückl E., Hausmann H., Mertl S., Meurers R., 2014. The 2013 Earthquake Series in the southern Vienna Basin: location. Advances in Geosciences 36, 77–80. https://doi.org/10.5194/adgeo-36-77-2014

Aschk K., 2005. IGME 5000: 1:5 Million International Geological Map of Europe and Adjacent Areas, Bundesanstalt für Geowissenschaften und Rohstoffe

Catchings R.D., Goldman M.R., Steidl J.H., Chan J.H., Allam A.A., Criley C.J., Ma Z., Langermann D.S., Huddleston G.J., McEvilly A.T., Mongovin D.D., Berg E.M., Ben-Zion Y., 2020. Nodal seismograph recordings of the 2019 Ridgecrest earthquake sequence. Seismological Research Letters 91/6, 3622–3633. https://doi.org/10.1785/0220200203

Chovanová Z., Kristek J., 2018. A local magnitude scale for Slovakia,

central Europe. Bulletin of the Seismological Society of America, 108/5A, 2756–2763. https://doi.org/10.1785/0120180059
Decker K., Peresson, H., Hinsch, R., 2005. Active tectonics and quaternary basin formation along the Vienna Basin Transform fault. Quat. Sci. Rev. 44, 305–320. https://doi.org/10.1016/j.quascirev.2004.04.012
Dunham A., Kiser E., 2020. Local earthquake tomography of the central Oregon forearc using a large-N, short duration, nodal array. Earth and Planetary Science Letters 551, https://doi.org/10.1016/j.epsl.2020.116559
Estève C., Liu Y., Koulakov I., Schaeffer A. J., Audet P., 2022. Seismic evidence for a weakened thick crust at the Beaufort Sea continental margin. Geophysical Research Letters 49/e2022GL100158. https://doi.org/10.1029/2022GL100158
Esteve C., Lu Y., Gosselin J. M., Kramer R., Bokelmann G., Götzl G., 2025. Seismic imaging of the southern Vienna Basin (Austria) using probabilistic ambient-noise tomography. Geophysical prospecting (under review). https://doi.org/10.22541/essoar.174703370.08315532/v1
Gosselin J.M., Biegel K., Hamidbeygi M., Dettmer J., 2023. Improvements in the regional earthquake focal mechanism catalogue for southwestern Yukon. In: Yukon Exploration and Geology 2022, K.E. MacFarlane (ed.), Yukon Geological Survey, 63–76.
Gutdeutsch R., Hammerl C., Mayer I., and Vocelka K., 1987. Erdbeben als historisches Ereignis – Die Rekonstruktion des niederösterreichischen Erdbebens von 1590, Springer Verlag Wien, Heidelberg, New York, 233 pp.
Froitzheim N., Plašienka D., Schuster R., 2008. Alpine tectonics of the Alps and Western Carpathians, The Geology of Central Europe Volume 2: Mesozoic and Cenozoic, T. McCann. https://doi.org/10.1144/CEV2P.6
Hausmann H., Hoyer S., Schurr B., Brückl E., Houseman G., Stuart G., 2010. New seismic data improve earthquake location in the Vienna Basin area, Austria. Austrian Journal of Earth Sciences 103/2, 2–14
Hinsch R., Decker K., Wagreich M., 2004. A short review of environmental tectonics of the Vienna Basin and the Rhine Graben area. Austrian Journal of Earth Sciences 94, 6–15
Hinsch R., Decker K., 2011. Seismic slip rates, potential subsurface rupture areas and seismic potential of the Vienna Basin Transfer Fault. International Journal of Earth Science, 100, 1925–1935. https://doi.org/10.1007/s00531-010-0613-3
Hintersberger E., Decker K., Lomax J., 2010. Largest earthquake north of the Alps excavated within the Vienna Basin, Austria, in: European Seismological Commission (ESC) 32nd General Assembly, Montpellier, France, Abstract T/Sd2/TU/05
Jiwani-Brown E.A., Koulakov I., Muñoz-Burbano F., Pacheco J.F., Mora M.M., Savard G., Lupi M., 2024. Subsurface anatomy of the Irazú–Turrialba volcanic complex, inferred from the integration of local and ambient seismic tomographic methods, Geophysical Journal International 237/2, 679–696, https://doi.org/10.1093/gji/ggae054
Koulakov I., 2009. LOTOS code for local earthquake tomographic inversion: Benchmarks for testing tomographic algorithms. Bulletin of the Seismological Society of America 99/1, 194–214. https://doi.org/10.1785/0120080013354
Koulakov I., D'Auria L., Prudencio J., Cabrera-Pérez I., Barrancos J., Padilla G. D., et al., 2023. Local earthquake seismic tomography reveals the link between crustal structure and volcanism in Tenerife (Canary Islands). Journal of Geophysical Research: Solid Earth 128/e2022JB025798. https://doi.org/10.1029/2022JB025798
Koulakov I., Sobolev S. V., 2006. Moho depth and three-dimensional P and S structure of the crust and uppermost mantle in the Eastern Mediterranean and Middle East derived from tomographic inversion of local ISC data. Geophysical Journal International 164/1, 218–235. https://doi.org/10.1111/j.1365-246X.2005.02791.x
Lenhardt W., Freudenthaler C., Lippitsch R., Fiegweil E., 2007. Focal-depth distributions in the Austrian Eastern Alps based on macroseismic data. Austrian Journal of Earth Sciences, 100, 66–79
Levi N., Weissl M., Decker K., 2024. Assessing the hazard of fault triggering by deep geothermal energy production in an active fault system via a 1D stress model and 3D fault mapping. International Journal of Earth Sciences (Geol Rundsch) 113, 583–609, https://doi.org/10.1007/s00531-023-02383-6
Mousavi S.M., Ellsworth W.L., Zhu W., Chuang L.Y., Beroza G.C., 2020. Earthquake transformer — an attentive deep-learning model for simultaneous earthquake detection and phase picking. Nature Communications 11, 3952. https://doi.org/10.1038/s41467-020-17591-w
Paige C.C., Saunders M.A., 1982. Lsqr: An algorithm for sparse linear equations and sparse least squares. ACM Trans. Math. Softw. 8/1, 43–71. https://doi.org/10.1145/355984.355989
Sachsenhofer R.F., Misch D., Rainer T., 2025. The Vienna Basin: petroleum systems, storage and geothermal potential. Geological Society, London, Special Publications 555/1, https://doi.org/10.1144/SP555-2023-205
Schmid F., Schlindwein V., Koulakov I., Plötz A., Scholz J.-R., 2017. Magma plumbing system and seismicity of an active mid-ocean ridge volcano. Scientific Reports 7/42949, https://doi.org/10.1038/srep42949
Schön J., 2015. Physical properties of rocks: Fundamentals and Principles of Petrophysics. Developments in Petroleum Science, Vol. 65, Amsterdam
Shearer P.M., Meng H., Fan W., 2023. Earthquake detection using a nodal array on the San Jacinto fault in California: Evidence for high foreshock rates preceding many events. Journal of Geophysical Research: Solid Earth 128, e2022JB025279. https://doi.org/10.1029/2022JB025279
Um J., Thurber C., 1987. A fast algorithm for two-point seismic ray tracing. Bulletin of the Seismological Society of America 77/3, 972–986. https://doi.org/10.1785/403BSSA077003097
Vasyura-Bathke H., Dettmer J., Steinberg A., Heimann S., Isken M.P., Zielke O., Mai P.M., Sudhaus H., Jónsson S., 2020. The Bayesian Earthquake Analysis Tool. Seismological Research Letters 2020 91/2A, 1003–1018. https://doi.org/10.1785/0220190075
Wessel P., Smith W.H.F., Scharroo R., Luis J., Wobbe F., 2013. Generic mapping tools: Improved version released. Eos 94, 409–410. https://doi.org/10.1002/2013EO450001
Woolam J., Münchmeyer J., Tilmann F., Rietbrock A., Lange D., Bornstein T., Diehl T., Giuschi C., Haslinger F., Jozinovic D., Michelini A., Saul J., Soto H., 2022. SeisBench – A Toolbox for Machine Learning in Seismology. Seismological Research Letters. https://doi.org/10.1785/0220210324
Zhu C., Beroza G.C., 2019. PhaseNet: a deep-neural-network-based seismic arrival-time picking method. *Geophysical Journal International* 216/1, 261–273, https://doi.org/10.1093/gji/ggy423
Zhu W., McBrearty I.W., Mousavi S.M., Ellsworth W.L., Beroza G.C., 2022. Earthquake phase association using a Bayesian Gaussian Mixture Model. Journal of Geophysical Research: Solid Earth 127/e2021JB023249. https://doi.org/10.1029/2021JB023249

Received: 15.5.2025
Accepted: 18.7.2025
Editorial Handling: Bastian Joachim-Mrosko